



University of Dundee

Factors affecting the procedure for testing cavitation erosion of GFRP composites using an ultrasonic transducer

Chernin, Leon; Guobys, Raimondas; Vilnay, Margi

DOI:
[10.1016/j.wear.2023.205059](https://doi.org/10.1016/j.wear.2023.205059)

Publication date:
2023

Licence:
CC BY-NC-ND

Document Version
Publisher's PDF, also known as Version of record

[Link to publication in Discovery Research Portal](#)

Citation for published version (APA):
Chernin, L., Guobys, R., & Vilnay, M. (2023). Factors affecting the procedure for testing cavitation erosion of GFRP composites using an ultrasonic transducer. *Wear*, 530-531, [205059].
<https://doi.org/10.1016/j.wear.2023.205059>

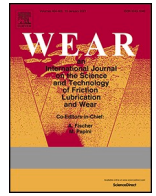
General rights

Copyright and moral rights for the publications made accessible in Discovery Research Portal are retained by the authors and/or other copyright owners and it is a condition of accessing publications that users recognise and abide by the legal requirements associated with these rights.

- Users may download and print one copy of any publication from Discovery Research Portal for the purpose of private study or research.
- You may not further distribute the material or use it for any profit-making activity or commercial gain.
- You may freely distribute the URL identifying the publication in the public portal.

Take down policy

If you believe that this document breaches copyright please contact us providing details, and we will remove access to the work immediately and investigate your claim.



Factors affecting the procedure for testing cavitation erosion of GFRP composites using an ultrasonic transducer

Leon Chernin^{*}, Raimondas Guobys, Margi Vilnay

School of Science and Engineering, University of Dundee, Dundee, UK

ARTICLE INFO

Keywords:

Ultrasonic cavitation erosion
Glass fibre reinforced polymer (GFRP) composite
Experimental setup and procedure
Specimen material properties

ABSTRACT

In many marine applications, glass fibre reinforced polymer (GFRP) composites are exposed to adverse environmental effects including cavitation. Prolonged exposure to cavitation can damage GFRP composite surfaces that would eventually require repairing or replacing marine device components. This study initially investigates the deterioration of GFRP composite and its constituent materials (i.e., epoxy and glass) by cavitation erosion. The cavitation cloud is produced by an ultrasonic transducer, and cavitation erosion tests adhered to ASTM G32-16 standard. It is shown that the erosion process of GFRP composite has characteristics of both epoxy and glass. The second part of this study investigates the effect of several parameters associated with the experimental setup, testing procedure and material properties on ultrasonic cavitation erosion of GFRP composite. These parameters include gas content in testing liquid, type of specimen support, specimen water absorption, acoustic impedance, and tensile strength. It is reported that specimen edge treatment influenced water absorption, specimen preconditioning was important for accurate recording of erosion damage accumulation, acoustic impedance and tensile strength were directly correlated with erosion damage, while the cavitation erosion process of GFRP composite was mostly insensitive to gas content in testing liquid but was significantly affected by the type of specimen support.

1. Introduction

The applications of glass fibre reinforced polymer (GFRP) composites are rapidly increasing due to their high strength and stiffness, low weight, and well-established and relatively easy manufacturing process. This leads to GFRP composites being subjected to various environmental effects and loads. In several specialised applications such as boat propellers, hydrofoils, and tidal turbine blades, GFRP composites are exposed to cavitation and can suffer from cavitation erosion. For example, Chernin and Val [1] showed that although the probability of cavitation is low, cavitation can develop on tidal turbine blades during short time periods that can add up to 51 days during a 10-year operation. Therefore, the resistance of GFRP composites to cavitation erosion is becoming a new concern for the design and maintenance of many marine devices.

A stationary specimen method used for studying the behaviour of polymers (including GFRP composites) exposed to cavitation erosion is based on the use of a 20 kHz frequency ultrasonic transducer that generates a cavitation cloud in a testing liquid (usually water). The original

testing method (i.e., the vibratory specimen method) was standardised in ASTM G32-16 [2] and was based on shaping a specimen as a button with a threaded shank. The outer diameter of the button is equal to that of the transducer tip horn. The specimen should be screwed directly into the horn. Manufacturing polymer specimens with such a shape represents a significant challenge. As a result, a stationary specimen method was used in several experimental works including Hammond et al. [3], Caccese et al. [4], Yamatogi et al. [5] and Guobys et al. [6] for testing GFRP composites and Hattori and Itoh [6] for testing plastics. In the stationary specimen method, GFRP specimens were positioned below a transducer horn that was equipped with a metal tip. Since the cavitation cloud would affect the tip as well, it was made of a cavitation-resistant material, e.g., titanium or stainless steel. The distance between the tip and the specimen and the peak-to-peak amplitude of the transducer tip should be carefully controlled. In addition to creating a cavitation cloud, the tip displaces the testing liquid and increases its temperature. The temperature of the liquid should also be controlled during testing because GFRP composites exhibit temperature sensitivity [8]. The increasing temperature decreases the peak load and increases fracture

^{*} Corresponding author.

E-mail address: l.chernin@dundee.ac.uk (L. Chernin).

energy due to the increasing ductility. The testing liquid temperature is usually maintained in the range between 23 °C and 27 °C [3–7].

The modifications to the ASTM G32-16 experimental procedure allowed for some variations in experimental setups, which could complicate the comparison of experimental results and lead to their misinterpretation and misleading conclusions. For example, Hammond et al. [3], Caccese et al. [4] and Yamatogi et al. [5] used a 0.5 mm distance between the transducer tip and the specimen surface. Hattori and Itoh [7] set this distance to 1 mm, while Guobys et al. [6] used a 0.8 mm distance based on the acoustic field pressure measurements. Hammond et al. [3] and Guobys et al. [6] set the peak-to-peak displacement amplitude of the ultrasonic transducer tip to 25 μm , while Caccese et al. [4], Yamatogi et al. [5] and Hattori and Itoh [7] used a 50 μm peak-to-peak tip displacement amplitude. Hammond et al. [3] used a metal (possibly aluminium or stainless steel) plate as specimen support, Caccese et al. [4] did not describe the specimen supporting structure, Yamatogi et al. [5] used a metal block, while Guobys et al. [6] used a stainless steel net frame. Hammond et al. [3], Caccese et al. [4] and Yamatogi et al. [5] did not explain the method used for fixing specimens in place during testing. Hattori and Itoh [7] did not describe their

experimental setup. From the schematic representation of the experimental setup, it can be assumed that Hammond et al. [3] glued specimens to metal plates, which were fastened to a metal frame. Based on the photographs in Yamatogi et al. [5], the specimens were most likely glued to metal blocks that were clamped to a metal base. Guobys et al. [6] fixed specimen corners to the stainless steel net, which was done to allow for easy dismounting and scanning of the specimens using X-ray computed tomography.

Yamatogi et al. [5], and Hattori and Itoh [7] used ion-exchanged water as a testing liquid, Hammond et al. [3] used artificial seawater, while Guobys et al. [6] used deionised water. Caccese et al. [4] did not mention the type of water they used in the tests. Gas content in the testing liquid was not discussed in the works considered. Preconditioning of FRP specimens in the testing liquid was applied by Guobys et al. [6] and neglected by Caccese et al. [4] and Yamatogi et al. [5]. Hammond et al. [3] tested both preconditioned and dry specimens. Only long-term water absorption with measurement intervals of a few weeks was considered by Hammond et al. [3]. Yamatogi et al. [5] eliminated the effect of water absorption on the weight of eroded specimens by measuring the composite mass loss using a filtration system with a mesh

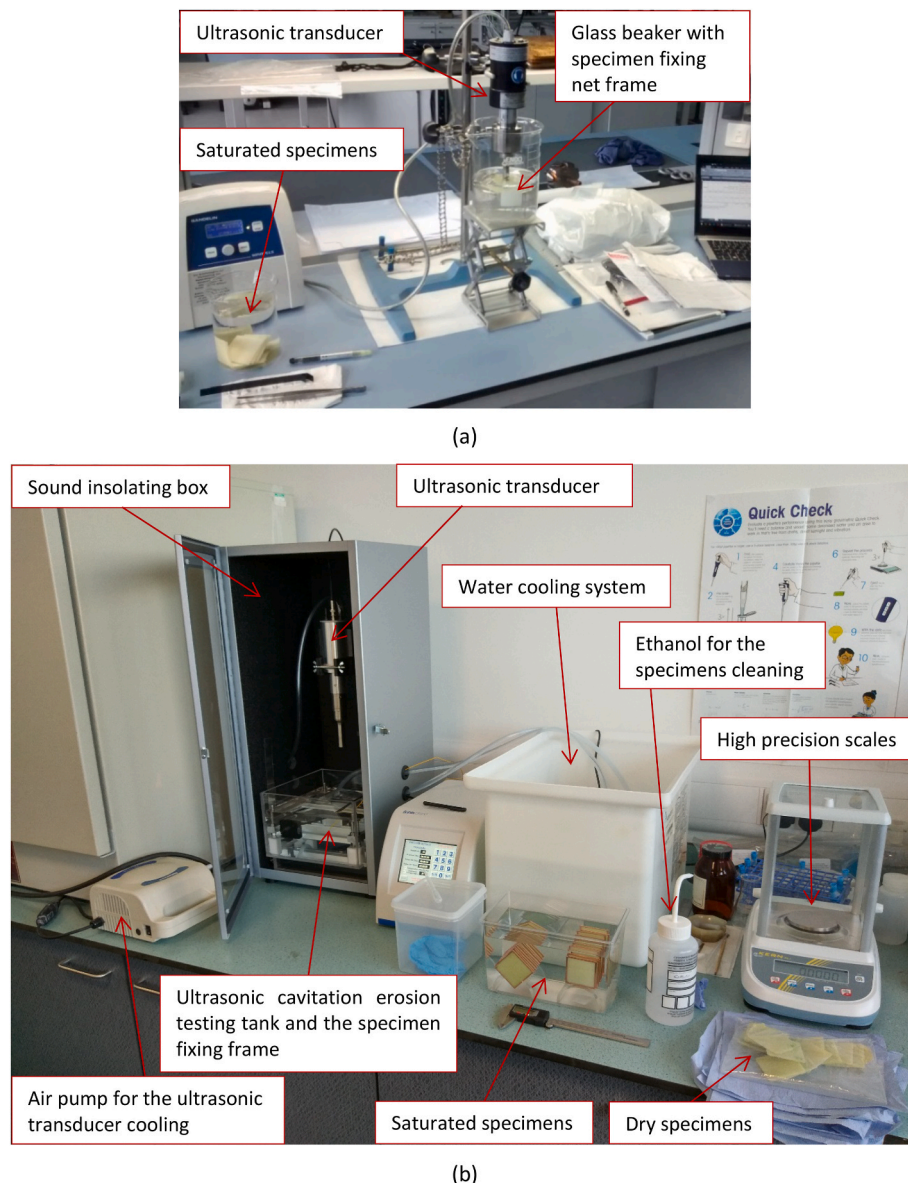


Fig. 1. Ultrasonic cavitation erosion test setups: (a) setup 1 and (b) setup 2.

size of 0.45 μm .

This paper has two objectives. The first objective is to study the behaviour of GFRP composite and its constituent materials (i.e., epoxy and glass) exposed to cavitation erosion. The second objective is to investigate the sensitivity of the ultrasonic cavitation erosion of GFRP composite to several parameters associated with the experimental setup, testing procedure and specimen material properties. This includes gas content in testing liquid, the type of specimen support, specimen water absorption, acoustic impedance, and tensile strength. Some parameters (e.g., gas content in testing liquid) showed insignificant influence on the ultrasonic cavitation erosion process, while others (e.g., the type of specimen support) affected the process severely.

2. Experimental methodology and materials

This section describes the methodology and materials used in the experimental programme.

2.1. Testing procedure

Ultrasonic cavitation erosion tests were conducted on stationary specimens in accordance with a modified testing procedure based on the ASTM G32-16 standard [2]. In these tests, GFRP composite specimens were exposed to cavitation clouds generated by an ultrasonic transducer leading to surface erosion. Ultrasonic cavitation erosion tests were performed with two different experimental setups (see Fig. 1) with different ultrasonic transducers, three amplifiers and three tip geometries. Setup 1 consisted of an ultrasonic transducer Bandelin HD3200, 1L glass beaker, laboratory stand, jack stand and a stainless-steel net frame for specimen placement (see Fig. 1a). The erosion tests were conducted using deionised water saturated with dissolved gas. Further information about setup 1 can be found in Guobys et al. [6]. Setup 2 consisted of an ultrasonic transducer Fisherbrand Q700, sound isolating box, testing tank with adjustable specimen clamping frame, water cooling system to maintain temperature within ASTM G32-16 standard [2] recommended range and the air pump for the ultrasonic transducer cooling (see Fig. 1b). The erosion tests were conducted using distilled water saturated with dissolved gas. In both experimental setups, the ultrasonic transducers were equipped with a 13 mm diameter tip, operated at 20 ± 0.5 kHz frequency and had a controllable peak-to-peak amplitude of the tip displacement. The distance between the transducer tips and the specimen surfaces was set to 0.8 mm. The erosion intensity of specimens was calibrated per the ASTM G32-16 standard [2] by setting the initial transducer amplitude to 25 μm and then increasing it to 50 μm . The tip peak-to-peak displacement of 50 μm resulted in the transducer tip velocity of 2 m/s.

The ultrasonic field generated by the transducer operating at 20 kHz frequency produced cavitation bubbles with a resonant radius (R_r) of 160 μm , which can be calculated by Minnaert resonance Eq. (1) [9] (overlooking surface tension and viscous attenuation):

$$R_r = \sqrt{\frac{3\gamma P_A}{\rho(2\pi f)^2}} \quad (1)$$

where γ is a heat capacity ratio, P_A is ambient pressure, ρ is water density, and f is frequency. Similar results were obtained in Refs. [10, 11] through experimental measurements.

In both experimental setups, the ultrasonic transducer induced vibrations to GFRP composite specimens and heavy mixing of water in a container. To prevent loss of material from edges (which were damaged by specimen cutting) during testing, handling and fixing in the testing frame, the edges of part of GFRP specimens were covered either with epoxy or copper tape, while a set of specimens was tested with free (uncovered) edges. The density of the epoxy covering the edges was 1110 kg/m^3 . The mass of the edge covering material was considered as part of specimens during erosion-induced mass loss calculations.

In the tests, the specimens were submerged 12 mm below the surface in a container filled with water. The setup 1 specimens were placed on a stainless-steel net frame, while the setup 2 specimens were placed on an aluminium block. In both cases, the specimens were fixed in the horizontal plane to prevent any displacements. The conductivity of deionised water in setup 1 was kept under 1 $\mu\text{S}/\text{cm}$ throughout testing, while the conductivity of distilled water was kept under 0.05 $\mu\text{S}/\text{cm}$ in Setup 2. To maintain the temperature at 25 ± 2 °C during the tests, the water in setup 1 was replaced at each measurement. In setup 2, the water was circulated between the testing tank and a cooling container using two water pumps. The temperature was monitored locally at the eroded specimen surface with a precision of ± 0.1 °C. It should be noted that in both test setups, the eroded material was not recovered as it would require a sophisticated filtration system similar to the one used in Ref. [5]. Instead, to eliminate a possible effect of eroded material on the process of cavitation erosion, the testing liquid was changed at regular intervals.

The schedule of mass loss measurements implemented in all erosion tests included two initial measurements taken at 5 min intervals followed by measurements at 10 min intervals. This method enabled the monitoring of the initial damage as well as the identification of erosion effects at all testing stages. At each measurement, the specimen surface was cleaned with ethanol and dried with a non-linting absorbent cloth. Control microscope examination of specimen surfaces after the application of the drying procedure showed that the non-linting absorbent cloth did not leave any residual fibres. The surface drying with a non-linting absorbent cloth removed surface moisture and the weighing procedure was very quick to allow for any significant changes in specimen weight due to the evaporation of absorbed water. A desiccator was not implemented because it was found to be slow in surface drying and demanded different time intervals to remove surface moisture in each test. The specimen mass was measured using scales with ± 0.1 mg precision. The eroded surfaces were examined with a digital microscope Olympus GX71 and photographed with a digital camera. The photographed eroded imprints were analysed with image processing software ImageJ [12] and specialised software VGStudio Max [13]. All specimens were scanned before and after the conclusion of testing using an X-ray computed microtomography system Nikon XT H 225 ST.

The cumulative mean depth of erosion (MDE) was calculated for each specimen using the mass loss (Δm) during cavitation erosion, specimen density (ρ_{FRP}) and specimen true eroded surface area (A), as shown in Eq. (2).

$$MDE = \frac{\Delta m}{\rho_{FRP} A} \quad (2)$$

2.2. Ultrasonic transducer calibration

Six specimens (S1–S6) made of Stainless Steel 316 (SS316) were used for calibration of the ultrasonic transducers as well as for comparative purposes. The density of SS316 was measured to be 7910 kg/m^3 . All specimens were cut to approximately 40 mm \times 40 mm squares and had a thickness of 2.95 mm. The specimen surfaces were mirror polished before cavitation erosion testing. The calibration was carried out following the ASTM G32-16 standard [2]. The specimens S2 and S3 were tested with setup 1, while the specimens S1 and S4–S6 were tested with setup 2. The experimental conditions were replicated by setting both ultrasonic transducers to similar power outputs to create similar ultrasonic field intensity. Furthermore, water temperatures and specimen boundary conditions were kept similar. Fig. 2 shows the results of cavitation erosion tests of the six SS316 specimens in terms of cumulative MDE (i.e., curves S1–S6) overlaid over the relevant data from ASTM G32-16 (i.e., curves A, B, C and D taken from Fig. X3.1 in Ref. [2]). As can be seen, curves S1–S6 are lower than curves A, B, C and D. The difference in the data varies in the range of about 1.5–7 depending on the exposure time. This difference can be explained by the effects of

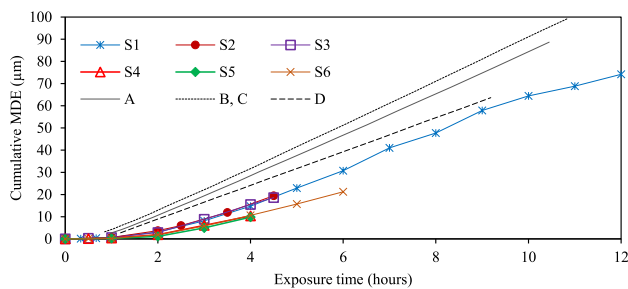


Fig. 2. Stainless Steel 316 cumulative mean depth of erosion over cumulative exposure time during ultrasonic transducer calibration (S1–S3 – specimen tested in gas-saturated testing liquid, S4–S6 – specimen tested in degassed testing liquid) and ASTM G32-16 Stainless Steel 316 cavitation erosion results (A, B, C, D) from different laboratories [2].

several factors. First, the erosion rate in the vibratory specimen method applied in the ASTM G32-16 tests the cumulative erosion rate is 3.6 times higher than in the stationary specimen method applied in this study [14]. Second, curves A, B, C and D represent the averaged data collected from several labs and obtained using specimens of different diameters and shapes (see clause X3.2.2 of [2]), which could explain the divergence of data. Curves S1-6 were obtained using ultrasonic horns of the same diameter and specimens of the same shape and dimensions. Third, the methodology for measurement of the eroded surface could have an additional influence on the results. In the current study, the true eroded surfaces were measured by means of specialised image processing software. Fourth, the cumulative MDE was calculated in the ASTM G32-16 data using the transducer tip area as the erosion imprint area (see Eq. (1)), while digital processing of erosion imprint images was used in this study for the accurate identification of damaged areas. Fifth, the data sets reported in the ASTM G32-16 standard lack incubation periods.

Specimens S1–S3 were eroded in gas-saturated testing water with a dissolved oxygen content of 8.8 mg/L, whereas specimens S4–S6 were tested in reasonably degassed testing liquid with a dissolved oxygen content of 6 mg/L. A significant difference is visible between the two specimen sets tested in different dissolved gas water environments. The average cumulative MDE after 4-h exposure time was higher in specimens S1–S3 by 56.6% than in specimens S4–S6. Specimens S1–S3 eroded quicker than specimens S4–S6 because of the influence of dissolved gasses on the cavitation erosion process. The erosion imprints generated in the gas-saturated water were uneven and contained large pits, whereas the erosion imprints generated in the degassed water were smooth and evenly distributed. This indicated the variation in the number and size of cavitation bubbles forming at the eroding surfaces. The gas-saturated testing water had a greater dissolved gas content. Therefore, the nucleation of cavitation bubbles was easier, which resulted in higher intensity of cavitation erosion.

2.3. Internal structure and mechanical properties of specimens

Specimens tested in this study were cut out of four sheets of glass fibre-reinforced polymer (GFRP) composite, which were also used in the previous study [6]. Sheets 1 and 2 had a target thickness of 2 mm, while sheets 3 and 4 had a target thickness of 4 mm. All sheets had bidirectional fibre distribution ($0^\circ/90^\circ$), with predominant $96\% \pm 1\%$ fibres orientation in the 0° direction. The percentage of the directional fibres was measured by separating and weighing fibres bundled in a glass fibre sheet supplied by the manufacturer of the GFRP composite sheets. According to the manufacturer, the composite sheets were made with a 50% fibre volume fraction. The fibre material was E-glass with standard mechanical properties. The E-glass fibre bundles were tied with small diagonal bundles of binding fibres. The binding fibres were made of a synthetic material (likely polyester) which melted when heated. Both surfaces of the GFRP sheets had smooth finish due to the use of a

vacuum-assisted resin transfer moulding (VARTM) technique with rigid flat mould surfaces.

Table 1 shows images of surfaces and cross-sections of specimens cut from the 4 GFRP sheets. The glass fibre bundles are oriented vertically in all images and can be distinguished by a darker colour. In contrast, the glass fibre bundles have a much lighter colour in the cross-sections. The inclined binding synthetic fibres can also be distinguished on the surface images. The internal structure, distribution and stacking of glass fibre bundles were analysed at different cross-sectional planes using X-ray computed microtomography imaging. The shapes of bundle cross-sections varied between an oval and a quadrilateral (parallelogram or rectangle) with rounded corners. The diameter of a single fibre on average was $19\ \mu\text{m}$, which was measured with a calibrated digital microscope (Olympus GX71). The average fibre bundle cross-section in specimens from sheet 1 was equal to 2.37 mm in width and 0.84 mm in height. The distance between bundles in a layer and the layers of bundles varied from 0 to 0.2 mm. In sheets 2, 3 and 4, the average fibre bundle cross-sections were equal to 3.28 mm in width and 0.87 mm in height. The distance between fibre bundles varied from 0 to 0.4 mm and between bundle layers from 0 to 0.2 mm.

The analysis of material properties and internal structure highlighted several differences between the GFRP composite sheets. Sheets 1 and 2 had approximately 2 mm thickness, while sheets 3 and 4 had approximately 4 mm thickness. In the same thickness group, sheet 3 had a 1.5% higher specific acoustic impedance due to a higher fibre volume fraction than sheet 4, while the specific acoustic impedance of sheet 1 was 3.9% higher than that of sheet 2. The microscope observations indicated that sheet 3 had the roughest surface with the largest initial scratches. X-ray microtomography showed that the epoxy between fibre bundles in sheet 4 was 50% wider near the surface than in sheet 3. Sheet 4 was 5% thicker than sheet 3 and had 25% thicker fibre bundles.

The mechanical properties of the GFRP composite provided by the manufacturer are presented in Table 2. The tensile strength and Young's modulus in 0° and 90° fibre orientation were validated based on ASTM D3039/D3039 M standard [15]. Table 3 presents the results of tensile tests including the means, standard deviations (St.Dev) and coefficients of variation (Coef.V) obtained based on 4 or 5 specimens in each case. As can be seen from the data in Tables 2 and 3, the strength of the specimens was either nearly equal to or lower than the values provided by the manufacturer, while the stiffness (Young's modulus) was higher. The differences between the tests and the manufacturer values could be attributed to the variation in the properties of constituent materials and in the fibre content of the specimens tested as well as to a more accurate testing method applied by the manufacturer.

Table 3 also provides the mean surface hardness of the 4 GFRP composite sheets measured using a Shore Durometer Type D in accordance with ASTM D2240 standard [16]. Since the surface of the unidirectional GFRP composite is inherently nonuniform due to the presence of fibre bundles and epoxy-filled gaps, the surface hardness was separately measured above (S_B) and between (S_E) fibre bundles. The S_B and S_E means were calculated based on the data reported in Ref. [6]. It was also observed that GFRP surface hardness was insensitive to prolonged saturation in water. Further details on the internal structure and properties of GFRP composite sheets and on the acoustic impedance testing procedure can be found in Ref. [6].

The response of GFRP composite to cavitation erosion was compared in this study with the response of pure epoxy. The pure epoxy specimens were cut from a sheet manufactured using commercially available epoxy. Table 4 shows the properties of this epoxy provided by the manufacturer. The density of the pure epoxy specimens was evaluated at $1158\ \text{kg/m}^3$ based on the volume estimated using the Archimedes' principle. As can be seen, the obtained density is at the upper end of the range provided by the manufacturer (see Table 4). The Shore D hardness of the pure epoxy specimens was measured at 84.5 HD, which was the low end of the range provided by the manufacturer.

Table 1
Surfaces and cross-sections of specimens cut from 4 GFRP sheets.


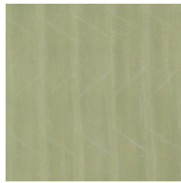
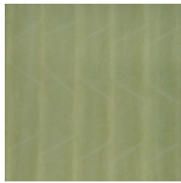
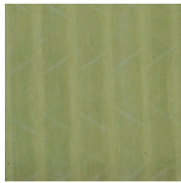




GFRP sheet	1	2	3	4
Surface				
Cross-section	 10 mm	 10 mm	 10 mm	 10 mm

Table 2
GFRP composite mechanical properties provided by the composite manufacturer.

	Strength, MPa	Modulus, GPa
Tensile 0	751.00	36.00
Tensile 90	52.00	11.00
Compression 0	747.20	38.10
Compression 90	175.90	11.30
In-plane shear	79.98	4.12
Flexure	786.37	34.50
Interlaminar Shear	65.74	–

Table 3
GFRP composite mechanical properties measured by the researchers.

Sheet	#	f_{t0} , MPa	E_0 , GPa	f_{t90} , MPa	E_{90} , GPa	S_B , HD	S_E , HD
GFRP 1	Mean	747.46	37.91	41.33	14.54	90.7	88.8
	St.Dev	25.20	1.43	2.41	0.31	–	–
	Coef.V, %	3.37	3.77	5.84	2.10	–	–
GFRP 2	Mean	748.34	42.10	39.84	13.65	92.1	85.7
	St.Dev	49.36	0.81	0.99	0.71	–	–
	Coef.V, %	6.60	1.93	2.48	5.18	–	–
GFRP 3	Mean	627.43	38.96	41.38	15.59	94.2	88.9
	St.Dev	40.54	1.01	0.90	0.60	–	–
	Coef.V, %	6.46	2.60	2.18	3.87	–	–
GFRP 4	Mean	624.50	39.27	56.57	15.41	92.7	87.1
	St.Dev	34.10	0.34	10.50	2.40	–	–
	Coef.V, %	5.46	0.86	18.56	15.60	–	–

In **Table 3**: f_{t0} and E_0 are the tensile strength and Young's modulus in specimens with 0° fibre orientation; f_{t90} and E_{90} are the tensile strength and Young's modulus in specimens with 90° fibre orientation; St.Dev is the standard deviation; Coef.V is the coefficient of variation (in %); S_B and S_E are the Shore D hardness of the GFRP specimen surface above and between fibre bundles, respectively.

2.4. Water absorption

Since FRP composites tend to absorb moisture [17–25], most of the specimens were preconditioned prior to testing. The preconditioning process included keeping the specimens in water until initial moisture equilibrium was reached. To analyse whether the specimen water intake might interfere with the mass loss capture during the ultrasonic cavitation erosion testing, several GFRP specimens were tested for water absorption in accordance with modified ASTM D5229/D5229 M and ASTM D570 standards [26,27].

In this study, specimens with three different edge conditions, including specimens with edges covered with epoxy, covered with

Table 4
Properties of epoxy provided by the epoxy manufacturer.

Property	Unit	from	to
Density AT30 hardener	kg/m ³	1040	
Density IN2 Epoxy resin	kg/m ³	1150	
Density combined 100:30	kg/m ³	1077	1165
Hardness 25 °C	Shore D/15	84.5	88.5
Glass transition temperature (peak)	°C	92	98
Water absorption (24h, 23 °C)	%	0.12	0.2
Water absorption (2h, 100 °C)	%	0.58	0.7
Flexural strength	MPa	112	124
Maximum strain	%	5	7
Strain at break	%	6	8
Flexural modulus	MPa	3150	3550
Tensile strength	MPa	65.5	73.5
Elongation at break	%	6	8

copper tape and left uncovered (i.e., free edges) were examined for water absorption. The uncovered edges were thoroughly cleaned with a fine brush and submerged in an ethanol bath to remove any potentially loose material before weighing and testing. The epoxy used for covering edges was degassed in a vacuum chamber prior to application to minimise the volume fraction of cavities. The specimens with epoxy-covered edges had an overall mass increase of less than 4%. The epoxy used for covering edges was also tested for water absorption, to check for a possible adverse effect of this technique on the accuracy of mass measurements during the erosion testing.

Before testing, uniform preconditioning of specimens was achieved by placing samples in an oven for 24 h drying period at 50 °C. The specimens were weighed before each procedure on scales with ± 0.1 mg precision. After the drying period, specimens were cooled in a sealable bag with no air and afterwards placed in water. Measurements were taken every 24 h. At all stages, the water temperature was kept constant. Specimens were placed vertically in slots of a holder to maximize surface contact with water. The water of different purity (i.e., deionised with a conductivity of <1 $\mu\text{S}/\text{cm}$ and distilled with a conductivity of <0.05 $\mu\text{S}/\text{cm}$) was used to test the effect of water purity on GFRP composite water intake. The effect of specimen size on the water absorption was tested using 13 mm and 50 mm square specimens with 2 mm and 4 mm thicknesses. These specimen dimensions were chosen based on two erosion techniques in ASTM G32-16 standard [2], the 13 mm diameter ultrasonic transducer tip and the glass beaker volume during initial testing using setup 1.

3. Results and discussion

3.1. Water absorption

Fig. 3 summarises the results of all water absorption tests carried out on 50 mm square specimens with 2 mm and 4 mm thicknesses (indicated by 't2' and 't4' in the legend, respectively). The edges of the specimens were covered either with epoxy or copper tape or left free (indicated by

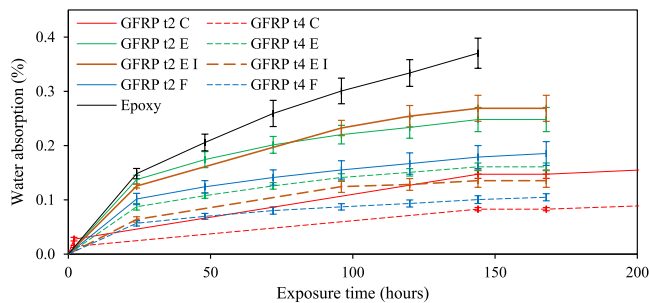


Fig. 3. Water absorption tests on pure Epoxy specimens and 2 mm-thick ('t2') and 4 mm-thick ('t4') GFRP specimens with free edges ('F') and edges covered by epoxy ('E') and copper tape ('C') submerged in deionised ('T') and distilled water. Average test results presented with a 95% confidence interval derived using Student's *t* distribution.

'E', 'C' and 'F' in the legend, respectively). Specimens with epoxy-covered edges were submerged in deionised and distilled water, while distilled water was used for testing all other specimens. The use of deionised water is indicated by 'T' in the legend of Fig. 3. In each of the 4 cases considered, 4 specimens from each of the 4 GFRP sheets were tested adding up to 64 GFRP specimens in total. As per ASTM D5229/D5229 M standard [26], the effective moisture equilibrium was reached in all specimens with covered edges after 144 h of submersion because the specimen weight did not change in the following measurement at 168 h of submersion. The most intensive water absorption occurred during the first 24 h of submersion, after which the rate of water absorption gradually decreased. By the end of the tests, the 2 mm-thick specimens absorbed about 8% more deionised water than distilled water, while the 4 mm-thick specimens absorbed about 16% more distilled water (see curves 'GFRP t2 E', 'GFRP t4 E', 'GFRP t2 E I', and 'GFRP t4 E I' in Fig. 3). Furthermore, the 2 mm-thick specimens absorbed about 50% more deionised water (in grams) and about 35% more distilled water than the 4 mm-thick ones. Therefore, the water purification technique could affect the GFRP composite water absorption.

Specimens with edges covered by copper tape absorbed distilled water at a much slower rate than the specimens with epoxy-covered edges (compare curves 'GFRP t2 C', 'GFRP t4 C', 'GFRP t2 E' and 'GFRP t4 E' in Fig. 3). After 144 h of submersion, the 2 mm-thick specimens with copper-taped edges absorbed 40% less water than the 2 mm-thick specimens with epoxy-covered edges. This difference increased to nearly 50% for 4 mm-thick specimens.

The specimens with free edges continued absorbing distilled water after 144 h of submersion without reaching an effective moisture equilibrium, although the rate of their water absorption decreased with prolonged exposure (see curves 'GFRP t2 F' and 'GFRP t4 F' in Fig. 3). During the tests, the specimens with free edges absorbed water slower than the specimens with epoxy-covered edges but faster than the specimens with copper-taped edges. After 144 h of submersion, the 2 mm-thick specimens with free edges absorbed 25% less water than the 2 mm-thick specimens with epoxy-covered edges and 21% more water than the 2 mm-thick specimens with copper-taped edges. This difference increased to 35% for the 4 mm-thick specimens with free and epoxy-covered edges but remained similar for the 4 mm-thick specimens with copper-taped edges.

In addition to the GFRP composite specimens, 4 specimens made of pure epoxy were tested in distilled water. The specimens had a 50 mm square shape and an average thickness of 4.4 mm. The results of these tests are given in Fig. 3 as curve 'Epoxy'. As can be observed, the pure epoxy specimens maintained a higher water intake than the GFRP specimens at all testing stages. However, the water absorption of the pure epoxy specimens at an early testing stage was comparable to that of the GFRP composite due to the initial absorption of water by the surface epoxy in both materials. After 144 h of saturation, the pure epoxy

specimens absorbed about 2.7 times more water than the 4 mm-thick GFRP specimens with free edges and about 1.4 times more water than the 4 mm-thick GFRP specimens with epoxy-covered edges (compare curves 'Epoxy', 'GFRP t4 F' and 'GFRP t4 E' in Fig. 3).

In all cases of specimen edge treatment, 2 mm-thick specimens absorbed more water than 4 mm-thick specimens regardless of the water purification technique used. It should be noted that water absorption of GFRP specimens with free edges after 7 days of exposure obtained in this study was similar to that reported in Hammond et al. [3]. The divergence between the experimental results at later testing stages can be explained by Hammond et al. [3] using linear interpolation for obtaining long-term water intake.

To check long-term water absorption behaviour, GFRP specimens with edges covered with copper tape were tested in distilled water for 212 days. The results of these tests are shown in Fig. 4, where each curve corresponds to specimens cut from one of the 4 GFRP sheets investigated in this study. Note that the data describing water absorption of these specimens at the early testing stage of up to 200 h of exposure can be seen in more detail in Fig. 3, where it is presented based on specimen thickness as curves 'GFRP t2 C' and 'GFRP t4 C'. Fig. 4 shows that after reaching a plateau between 144 h and 168 h of submersion (which is defined by ASTM D5229/D5229 M standard [26] as an effective moisture equilibrium), the specimens continued absorbing water at a gradually decreasing rate. The 2 mm-thick specimens (see curves 'GFRP 1 C' and 'GFRP 2 C') absorbed more water than the 4 mm-thick specimens (see curves 'GFRP 3 C' and 'GFRP 4 C') at all testing stages. Specimens from sheets 1 and 3 absorbed more water but exhibited higher data variation than their counterparts from sheets 2 and 4. After 16 days of submersion, the specimens increased their thickness by up to 0.02 mm on average, while the dimension perpendicular to fibre bundle orientation increased up to 0.05 mm on average. In contrast, the specimen dimension parallel to the fibre bundle orientation underwent insignificant changes. These non-uniform dimensional changes agree with the anisotropic heterogeneous properties of the unidirectional GFRP composite.

Fig. 5 shows the water absorption data after 24-h saturation collected for 2 mm and 4 mm thick specimens (indicated by 't2' and 't4', respectively) with 13 mm and 50 mm edge lengths (indicated by 'L13' and 'L50', respectively) and free and epoxy-covered edges (indicated by 'F' and 'E', respectively). This testing period was analysed in more detail due to the highest water absorption rates observed. The average surface areas are also given in Fig. 5 for each specimen group. The water absorption data was shown with a 95% confidence interval obtained from Student's *t* distribution. To allow for comparison between specimens of different sizes, the water absorption data were normalised against specimen surface area. As can be seen, the percentile water absorption of small specimens with free edges (see data sets 't2-L13-F' and 't4-L13-F') was almost twice higher than that of the large specimens (see data sets 't2-L50-F' and 't4-L50-F'), while the size difference between these specimens was about 3.8 times. The variation in water absorption values

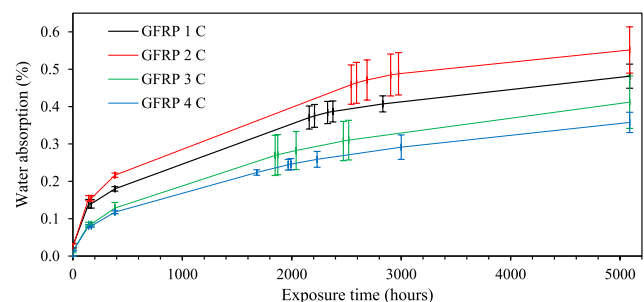


Fig. 4. Long-term water absorption test on GFRP specimens with edges covered by copper tape submerged in distilled water. Average test results presented with a 95% confidence interval derived using Student's *t* distribution.

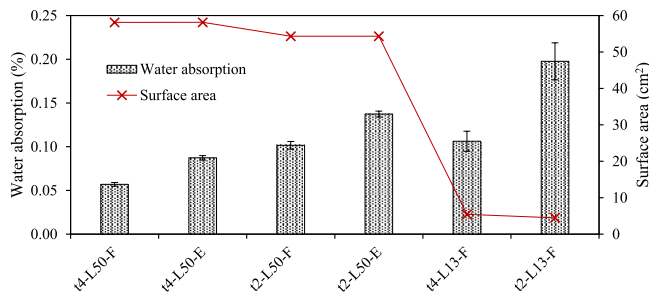


Fig. 5. Water absorption after 24-h saturation and corresponding surface areas of 2 mm-thick ('t2') and 4 mm thick ('t4') GFRP specimens with free ('F') and epoxy-covered ('E') edges of 13 mm ('L13') and 50 mm ('L50') lengths.

was significantly smaller in the large specimens. The 2 mm-thick specimens absorbed more water than the 4 mm-thick specimens regardless of edge condition or specimen size. Additionally, edge covering with epoxy resulted in a 53% increase in water absorption in the 4 mm-thick specimens and in a 35% increase in the 2 mm-thick specimens.

Based on the above discussion, it can be concluded that covering specimen edges with copper tape was the most efficient edge treatment method. The use of epoxy for edge covering requires adequate preconditioning in testing liquid. Water absorption was influenced by water purity and specimen size. It should be noted that Hammond et al. [3] reported a similar conclusion that water absorption of GFRP composite after 24-h exposure was affected by specimen size.

3.2. Cavitation erosion of saturated specimens

The results of ultrasonic cavitation erosion tests on GFRP specimens preconditioned in distilled water are depicted in Fig. 6 in terms of the cumulative mean depth of erosion (MDE) versus exposure time. The results of these tests were obtained using setup 2. All specimens had a 50 mm square shape and were tested on an aluminium block in reasonably degassed water. The edges of specimens were covered with copper tape. The number in curve names in Fig. 6 legend stands for the GFRP sheets from which tested specimens were cut out. Each curve was calculated as an average for 4 same sheet specimens tested. The average value curves fall within each other's 95% confidence intervals. Since all the average value curves had a similar shape, all specimens developed erosion damage in a similar manner. MDE increased slowly up to 20 min of exposure. This response is associated with the initial removal of the epoxy covering layer above the fibre bundle. Once the epoxy layer was removed, the erosion process accelerated due to the faster removal of fibres. This is reflected in a quick increase of MDE between 20 and 100 min of exposure. After 100 min, the damage accumulation process

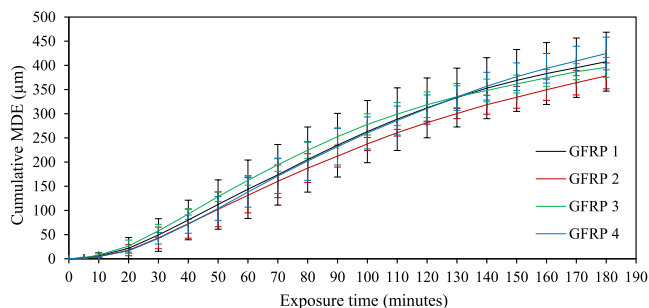


Fig. 6. Cumulative mean depth of erosion versus cumulative exposure time for GFRP specimens subjected to ultrasonic cavitation erosion on an aluminium block in reasonably degassed water. Edges of specimens were covered with copper tape. Average results are depicted with a 95% confidence interval derived using Student's t distribution.

developed slower. The highest variation in MDE occurred in sheet 1 specimens, whereas the highest difference in MDE values developed between specimens from sheets 2 and 3. It should be noted that SS316 specimens outperformed GFRP composites in the cavitation erosion resistance by several orders of magnitude of cumulative MDE (see Fig. 2).

Fig. 7 presents the variation of cumulative erosion rate with exposure time, where the cumulative erosion rate was calculated for the tested GFRP specimens by dividing cumulative MDE by cumulative exposure time. It can be concluded based on the shape of the average value curves that erosion rates developed similarly in all specimens. The initial increase in cumulative erosion rate was relatively linear for up to 30 min of exposure, indicating a short incubation period. The largest variation in erosion rates was reached at approximately 60 min of exposure. The variation diminished after about 120 min of exposure. The maximum cumulative erosion rate was reached in the interval between 82.5 and 117.5 min with the average maximum at about 100 min of exposure to cavitation. After peaking, the cumulative erosion rate decreased relatively linearly. This behaviour can be attributed to two factors. First, the distance between the specimen surface and the ultrasonic transducer tip increased due to surface erosion resulting in the reduction of erosion intensity of the cavitation cloud generated. Second, the complex structure of the eroding surfaces localised and mitigated the erosive effect of the ultrasonic cavitation cloud [6].

3.3. Parameters influencing the erosion process

This section summarises the investigation of the effects of several parameters on the GFRP composite performance in ultrasonic cavitation erosion tests, which were carried out using both setups 1 and 2. The parameters can be divided into those associated with the experimental setup and procedures and those associated with the specimen properties. The first group of parameters (i.e., those associated with the experimental setup and procedures) include specimen preconditioning, gas content in testing liquid and type of specimen support. The second group of parameters include material composition, specific acoustic impedance and tensile strength. Unless otherwise specified, the experimental results presented in this section were obtained using setup 2. All specimens had a 50 mm square shape. Edges of all specimens tested in setup 1 were covered with epoxy, while those tested in setup 2 were covered with copper tape. All saturated specimens were preconditioned to eliminate water absorption by the composite matrix and edge-covering epoxy (if present).

3.3.1. Effect of specimen preconditioning and material composition

Dry GFRP composite specimens were tested under identical erosion conditions as the saturated specimens to establish the effect of specimen preconditioning on the cavitation damage recording. The average

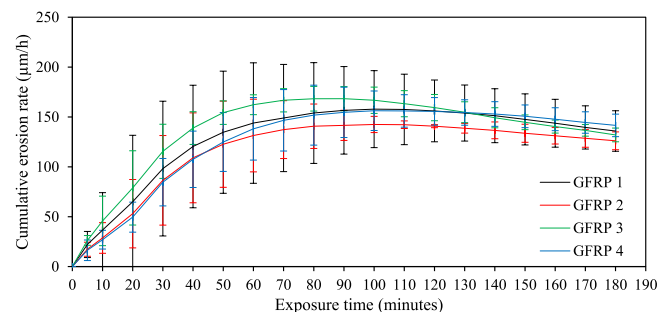


Fig. 7. Cumulative erosion rate versus cumulative exposure time for GFRP specimens subjected to ultrasonic cavitation erosion on an aluminium block in reasonably degassed water. Edges of specimens were covered with copper tape. Average results are shown with a 95% confidence interval derived using Student's t distribution.

cumulative MDE of 4 dry specimens (one from each GFRP sheet) is presented in Fig. 8 as curve 'GFRP D'. It can be observed that the MDE was negative during the first 20 min of testing, indicating a mass gain of the dry specimens associated with water intake. Between 20 and 30 min of testing, MDE developed slowly in the dry specimens. To establish the difference in the erosion processes of dry and saturated specimens, the cumulative MDE data from Fig. 6 averaged for all preconditioned GFRP specimens is also shown in Fig. 8 as curve 'GFRP'. It can be observed that the erosion processes developed similarly in the dry and saturated specimens after 30 min of testing. MDEs of the dry specimens were offset (i.e., the curves shifted downwards in the diagram) by the initial mass gain induced by water absorption. It seems that water absorption was important at the beginning of the tests, as the curves of both dry and saturated composites are parallel at later erosion stages.

Since the GFRP composite consisted of epoxy and glass fibres, the response of specimens made from the constituent materials to cavitation erosion was also investigated. Fig. 8 depicts the results of the test on pure epoxy and pure glass specimens (see curves 'Epoxy' and 'Glass'). Four pure epoxy specimens and one glass specimen were tested. The pure epoxy specimens had a 50 mm square shape and were 4.4 mm thick. The properties of the epoxy used in manufacturing the pure epoxy specimens are given in Table 4. The pure epoxy specimens were preconditioned in distilled water during water absorption tests (see Section 3.1). The pure glass specimen of 64 mm square shape was cut out from a 3.85 mm-thick sheet of float glass. As can be seen in Fig. 8, the GFRP composite and the pure epoxy eroded in a similar way until about 30 min of exposure, after which the GFRP composite eroded faster. This phenomenon occurred because cavitation initially eroded the epoxy matrix in the GFRP composites until glass fibres were sufficiently uncovered. The erosion process of the glass specimen was substantially quicker overtaking the GFRP and pure epoxy specimens after 5 min and reaching a steady state after 30 min of testing. This behaviour indicated the importance of material hardness and brittleness for cavitation erosion resistance. The pure epoxy and glass specimens defined the lower and upper limits for the cavitation erosion of GFRP composite, the resistance to which would depend on the fractions and arrangement of material constituents in the composite.

A better demonstration of the initial mass gain effect in the dry GFRP specimens is presented in Fig. 9, where the curves show average values of cumulative erosion rates. As can be seen, the cumulative erosion rate of dry specimens was negative during the first 10–15 min of exposure. This phenomenon is the result of the mass gain by the dry specimens due to the water intake accelerated by the ultrasonic field. The erosion rate gradually increased with exposure time reaching its maximum at the end of testing. Fig. 9 also presents the test data from Fig. 7 averaged for all saturated specimens. The curves of the dry and saturated specimens

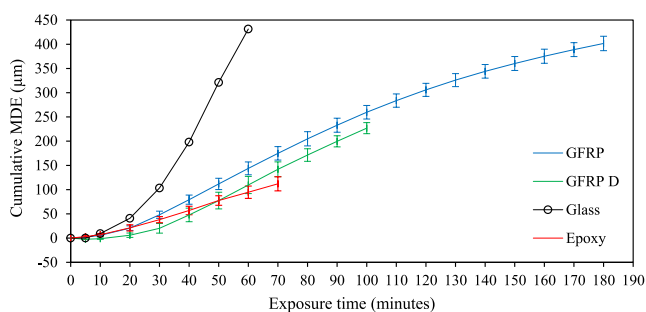


Fig. 8. Cumulative mean depth of erosion versus cumulative exposure time for GFRP, pure glass and pure epoxy specimens subjected to ultrasonic cavitation erosion on an aluminium block in reasonably degassed water. GFRP and Epoxy specimens were saturated (preconditioned) before testing. GFRP D specimens were tested unsaturated (dry). Edges of GFRP and GFRP D specimens were covered with copper tape. Average results are shown with a 95% confidence interval derived using Student's t distribution.

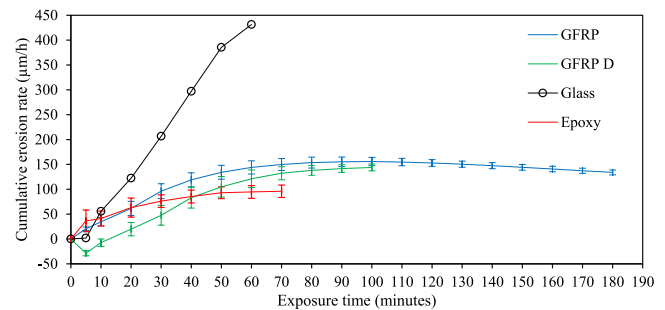


Fig. 9. Cumulative erosion rate versus cumulative exposure time for GFRP, pure glass and pure epoxy specimens subjected to ultrasonic cavitation erosion on an aluminium block in reasonably degassed water. GFRP and Epoxy specimens were saturated (preconditioned) before testing. GFRP D specimens were tested unsaturated (dry). Edges of GFRP and GFRP D specimens were covered with copper tape. Average results are shown with a 95% confidence interval derived using Student's t distribution.

diverged at the initial testing stages, after which they began converging. The erosion rates at 100 min of testing remained slightly lower in the dry specimens. Therefore, preconditioning of GFRP composite is especially important for the initial stages of ultrasonic cavitation erosion. The effect of water absorption gradually diminished in the advanced erosion stages. The qualitative development of cavitation erosion was similar in both the dry and saturated composites.

Fig. 9 also shows the development of cumulative erosion rates in the specimens made of pure epoxy and pure glass. The erosion rates of saturated GFRP composite and pure epoxy were relatively close in the first 20 min of exposure. There was an initial increase in the erosion rate of the pure epoxy specimens relative to the GFRP specimens during the first 5 min of exposure accompanied by increased data variation and confidence interval. This phenomenon was the result of a sudden local temperature increase in some pure epoxy specimens, which resulted in the formation of surface microcracks. The reason for this behaviour was not conclusive. After 20 min of exposure, the erosion rate in the GFRP composite became larger than in the pure epoxy due to the erosion of glass fibres in exposed bundles. The glass specimen demonstrated an incubation period of 5 min (represented by a very low erosion rate) due to an extremely smooth surface. During this period no measurable material loss was registered. Once cavitation formed rough surface topography, the erosion rate increased linearly and rapidly. After 10 min of exposure, the erosion rate of the glass was the highest among the materials considered. The erosion rate developed in the GFRP composite with rapid increase and slow decrease after reaching the peak at about 80 min of testing. The erosion rates in the glass and pure epoxy specimens did not reach the peak during their testing periods, although the increase in the erosion rate of epoxy was very slow by the end of testing. A good agreement between 'GFRP' and 'Epoxy' curves in Fig. 9 during the first 20 min of exposure indicated the initial dominance of surface epoxy erosion. The following divergence in the 'GFRP' and 'Epoxy' curves indicated the increasing importance of the erosion of glass fibres since the glass specimen eroded significantly faster. The comparison between the pure epoxy, GFRP and glass specimens shows that the curves of the glass and epoxy represent boundaries for the GFRP composite. Furthermore, the comparison of the cumulative erosion rates and surface hardness of pure epoxy, GFRP composite, and glass (listed in the order of increasing surface hardness) suggests that during a well-established cavitation erosion process, a higher surface hardness corresponds to a higher cavitation erosion rate and surface damage. This conclusion can be explained by higher impact energy absorption and lower energy dissipation by the material.

3.3.2. Effect of gas content in testing liquid

The ASTM G32-16 standard [2] does not provide any specific

guidance on gas content in the testing liquid. It only mentioned in Note 4 the importance of gas content stabilisation for the first 30 min of the erosion process. The effect of gas content in a testing liquid on ultrasonic cavitation erosion intensity was observed in this study during the calibration of the ultrasonic transducers (see Section 2.1). This phenomenon was investigated further using 4 GFRP specimens (one per each GFRP sheet) and distilled water with a conductivity of $<0.05 \mu\text{S}/\text{cm}$ and dissolved oxygen content of $8.8 \text{ mg}/\text{L}$. All specimens were preconditioned prior to testing. The water distillation process included boiling, a stabilisation period and gas saturation by pumping air through. The oxygen content was measured in the liquid with a dissolved oxygen meter, which was calibrated in $0 \text{ mg}/\text{L}$ dissolved oxygen liquid and further checked in nitrogen-saturated distilled water.

Fig. 10 depicts the average cumulative MDEs from the 4 ultrasonic cavitation erosion tests in gas-saturated water together with the tests in reasonably degassed water with an oxygen content of $6 \text{ mg}/\text{L}$ discussed in Section 3.2.1 (see Fig. 6). As can be seen, the considered gas content in the testing liquid had an insignificant influence on the cumulative MDE, although the variability of results was larger for the specimens tested in gas-saturated water.

The cumulative erosion rates are illustrated in Fig. 11 for the tests carried out in gas-saturated and reasonably degassed water. It can be observed that gas saturation slightly influenced the average erosion rates during the first 20 min of testing, while its effect in the later testing stages was insignificant. In contrast, the variability of cumulative erosion rate values increased significantly at all testing stages.

It is necessary to note that the insignificance of the effect of gas content in the testing liquid on the ultrasonic cavitation erosion of GFRP composite comparably to that of Stainless Steel 316 can potentially be attributed to different erosion mechanisms developing in both materials. This conclusion is supported by a highly non-uniform erosion imprint and a relatively high rate of the erosion process of GFRP composite (see Section 3.4 as well as [3,6]). In contrast, the erosion imprint of SS316 specimens was relatively uniform and the erosion process was reasonably slow.

3.3.3. Effect of specimen support

Hammond et al. [3] glued GFRP specimens to a metal plate, while Yamatogi et al. [5] glued them to a metal block. This type of specimen support prevented scanning the specimens using X-ray computed microtomography for a detailed examination of the internal damage done to the specimen surface by cavitation. To eliminate this drawback, an alternative type of specimen support was used by Guobys et al. [6].

The influence of specimen support characteristics on the process of ultrasonic cavitation erosion of preconditioned GFRP specimens was investigated in this section using both setup 1 and 2. Setup 1 was used with a stainless steel net frame as specimen support, while specimens

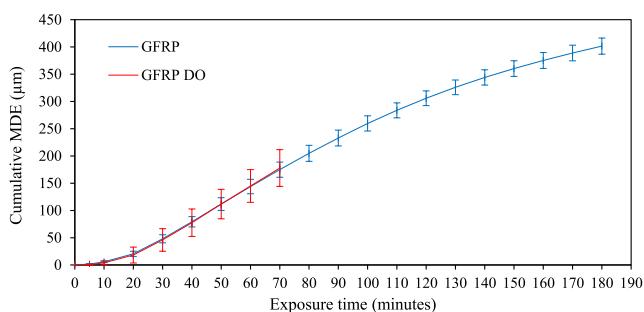


Fig. 10. Cumulative mean depth of erosion versus cumulative exposure time for GFRP specimens subjected to ultrasonic cavitation erosion on an aluminium block in reasonably degassed and gas-saturated (indicated by 'DO' in the legend) water. Edges of all specimens were covered with copper tape. Average results are shown with a 95% confidence interval derived using Student's *t* distribution.

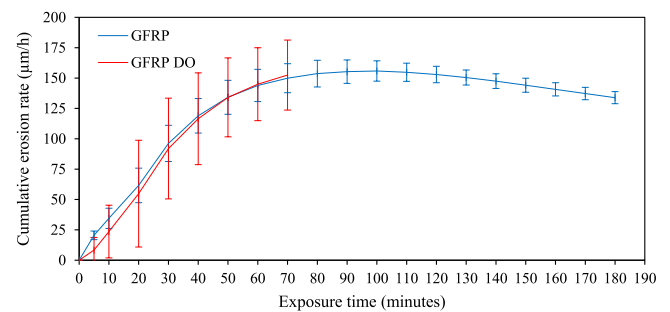


Fig. 11. Cumulative erosion rate versus cumulative exposure time for GFRP specimens subjected to ultrasonic cavitation erosion on an aluminium block in reasonably degassed and gas-saturated (indicated by 'DO' in the legend) water. Edges of all specimens were covered with copper tape. Average results are shown with a 95% confidence interval derived using Student's *t* distribution.

were supported in setup 2 using either an aluminium block or a 5 mm thick neoprene sheet placed within an aluminium clamping frame. 8 GFRP specimens (two per each GFRP sheet) were tested on the stainless steel net frame and 4 GFRP specimens (one per each GFRP sheet) were tested on the neoprene sheet. The data for the specimens tested on the aluminium block was taken from Section 3.2.1 (see Fig. 6), while the data for the specimens tested on the stainless steel net frame was taken from Guobys et al. [6]. The erosion results are summarised in Fig. 12 in terms of average cumulative MDE depending on specimen thickness and the type of specimen support. In the legend, 't2' and 't4' indicate 2 mm-thick and 4 mm-thick specimens, while 'A', 'N' and 'S' mean the aluminium block, the neoprene sheet and the stainless steel net frame, respectively. 95% confidence intervals derived using Student's *t* distribution are shown for the specimens tested on the aluminium block and a stainless steel net frame. The number of specimens tested on the neoprene sheet was too low (i.e., 2 per curve) for confidence interval calculations.

As can be seen in Fig. 12, there is a correlation between the type of specimen support, specimen thickness and erosion damage. The thickest (i.e., 4 mm thick) specimens tested on the stiffest support (i.e., the aluminium block) developed the highest erosion damage (see 'GFRP t4 A' curve). This phenomenon can be explained by the synergetic influence of the specimen thickness (which increases specimen bending stiffness) and the specimen support stiffness on the amplitude of GFRP specimen vibration introduced by the ultrasonic transducers during testing. Both higher thickness and higher support stiffness limited the vibration amplitude, thus more bubbles in the cavitation cloud collapsed close enough to the specimen surface to cause damage. Furthermore, the

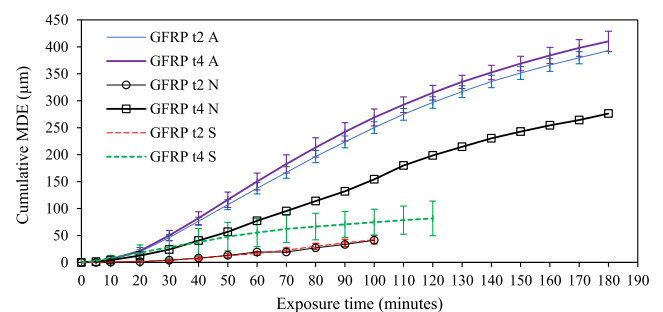


Fig. 12. Cumulative mean depth of erosion versus cumulative exposure time for 2 mm-thick ('t2') and 4 mm-thick ('t4') GFRP specimens subjected to ultrasonic cavitation erosion in reasonably degassed water on an aluminium block ('A'), a neoprene sheet ('N'), and a stainless steel net frame ('S'). Edges of GFRP A and N specimens were covered with copper tape. Edges of GFRP S specimens were covered with epoxy. Average results are shown with a 95% confidence interval derived using Student's *t* distribution.

ultrasonic cavitation cloud was the most aggressive at a certain distance from the transducer tip (e.g., this distance equals 0.5 mm for Fisherbrand Q700 used in setup 2). A smaller amplitude of specimen vibration increased the time during which the specimen surfaces were exposed to the region with the most aggressive cavitation in the ultrasonic cavitation cloud.

Specimen thickness had a proportionally smaller effect on erosion damage for specimens tested on stiffer support, e.g., the difference between MDE curves for 2 mm-thick and 4 mm-thick specimens is smaller for the specimens tested on the aluminium block (compare 'GFRP t2 A' and 'GFRP t4 A' curves in Fig. 12). The similarity of the MDE curves of the 2 mm-thick specimens tested on the neoprene sheet and stainless steel net frame (i.e., 'GFRP t2 N' and 'GFRP t2 S' curves) signifies a similar process of their erosion. Consequently, the stiffness of both support systems was comparable. A twofold increase in specimen thickness resulted in a significant increase (by several times) in erosion damage for both support systems, thus indicating that the effect of thickness on specimen vibration was higher than that of support stiffness. The average MDE curves of the 4 mm-thick specimens (i.e., 'GFRP t4 N' and 'GFRP t4 S' curves in Fig. 12) diverged after 40 min of testing. It should be noted that the 'GFRP t4 N' curve was in the confidence interval of 'GFRP t4 S' curve up to 70 min of testing. This divergence could be attributed to a higher influence of the differences in the experimental setups (e.g., the specimen fixation mechanism in setup 2 was more reliable), which is supported by a high data variation of 'GFRP t4 S' curve.

Fig. 13 shows the effects of specimen thickness and support stiffness on the cumulative erosion rates of GFRP specimens subjected to ultrasonic cavitation. As can be seen, the support stiffness influenced the erosion process. The specimens on the stiff aluminium block (see 'GFRP t2 A' and 'GFRP t4 A' curves) eroded significantly faster over the entire testing period than the specimens on other supports. The only exception was the 4 mm-thick specimens tested on the stainless steel net frame that showed the fastest erosion during the first 20 min of testing (see 'GFRP t4 S' curve in Fig. 13). The erosion rates of the specimens tested on the stiff aluminium block steadily increased over the first 100 min of testing, after which it gradually declined. The specimens tested on the other supports (with the exception of the 4 mm-thick specimens tested on the stainless steel net frame) showed a much lower increase in the erosion rate over a longer period, e.g., reaching the peak value at 120 min for the 4 mm-thick specimens on the neoprene sheet (see 'GFRP t4 N' curve in Fig. 13). The erosion rates of the 2 mm-thick specimens tested on the neoprene sheet and the stainless steel net frame developed similarly over the entire testing period and did not reach their maximum (see 'GFRP t2 N' and 'GFRP t2 S' curves). The twofold increase in specimen thickness had an insignificant effect on the erosion rates in the specimens tested on

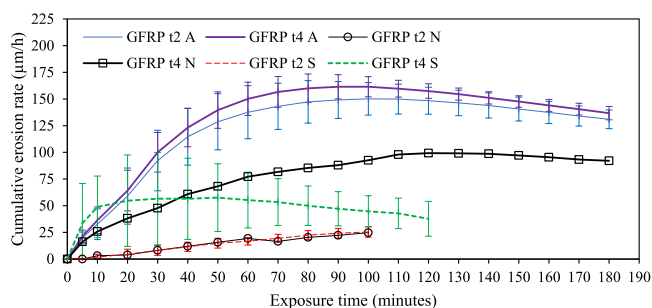


Fig. 13. Cumulative mean depth of erosion versus cumulative exposure time for 2 mm-thick ('t2') and 4 mm-thick ('t4') GFRP specimens subjected to ultrasonic cavitation erosion in reasonably degassed water on an aluminium block ('A'), a neoprene sheet ('N'), and a stainless steel net frame ('S'). Edges of GFRP A and N specimens were covered with copper tape. Edges of GFRP S specimens were covered with epoxy. Average results are shown with a 95% confidence interval derived using Student's t distribution.

the stiff aluminium block. Both 'GFRP t2 A' and 'GFRP t4 A' curves are close to each other and are in each other's confidence intervals. In contrast, erosion accelerated significantly in the thicker specimens tested on the more flexible supports. The differences in the erosion processes of the 4 mm-thick specimens tested on the neoprene sheet and the stainless steel net frame can also be seen from the comparison of 'GFRP t4 N' and 'GFRP t4 S' curves in Fig. 13. The erosion of the 4 mm-thick specimens tested on the stainless steel net frame accelerated significantly during the first 10 min of exposure to cavitation, after which it gradually decreased. The average erosion rate of the specimens on the neoprene sheet became higher than that of the specimens on the stainless steel net frame after 40 min of testing, while 'GFRP t4 N' curve remained in the confidence interval of 'GFRP t4 S' curve for up to 60 min of testing. The confidence interval of 'GFRP t4 N' curve was large, especially at the initial and intermediate stages of testing suggesting large variations in the rate of the erosion process in different 4 mm-thick specimens. It can be concluded from the above discussion that the higher flexibility of the experimental setup and the specimen slowed down the erosion process.

GFRP specimens were tested on the neoprene sheet in distilled water with a conductivity of $<0.05 \mu\text{S}/\text{cm}$, while deionised water with a conductivity of $<1 \mu\text{S}/\text{cm}$ was used for testing GFRP specimens on the stainless steel net frame. As a result, the erosion process (in terms of both cumulative MDE and erosion rate) of 2 mm-thick GFRP specimens was insensitive to water purity, while the effect of water purity on 4 mm-thick specimens was less clear.

The effect of GFRP specimen thickness on the stiffness of a testing setup in the ultrasonic cavitation erosion tests was investigated using 2 mm and 4 mm thick GFRP specimens and a 5 mm-thick neoprene sheet. In addition, a 1 mm-thick aluminium specimen was tested to provide a benchmark due to its high stiffness. All specimens had dimensions similar to those used in the cavitation erosion tests. The specimens on the neoprene sheet were subjected to static compression load. The load was applied at the specimen centre over a circular metal cylinder with 13 mm diameter, which was similar to the diameter of the ultrasonic transducer tip. The applied load and out-of-plane displacement were recorded and used for calculating the stiffness of the specimen-support system as a local slope of the load-displacement curve. Since the contribution of the neoprene sheet to the stiffness of the specimen-support system can be considered minor, the out-of-plane stiffness of the specimen defined the system response. Therefore, the system strain was calculated as a ratio between the recorded displacement and the initial thickness of the neoprene sheet. This methodology allowed for isolate the contribution of the specimen stiffness to the specimen-support system by eliminating the effect of specimen thickness. Fig. 14 illustrates the development of out-of-plane stiffness with compressive strain in the specimen-support system. Each curve in the figure represents an average of two tests on different specimens. As can be seen in Fig. 14, the stiffness of the aluminium specimen-support system was higher than that of the 4 mm-thick GFRP specimen-support system in the

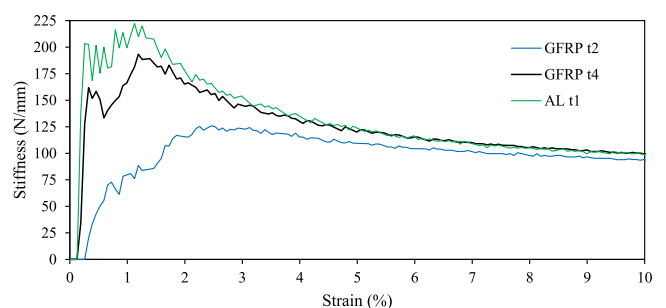


Fig. 14. Stiffness versus strain for 2 mm-thick ('t2') and 4 mm-thick ('t4') GFRP and 1 mm-thick ('t1') aluminium ('AL') specimens tested on a 5 mm-thick neoprene sheet under compression load.

strain range between 0 and 3%, after which the stiffnesses of both systems became similar. The 2 mm-thick GFRP specimen-support system had substantially lower stiffness at the strains of up to about 6%. In the low strain range, the specimen-support system with the 4 mm-thick GFRP specimen was about two times stiffer than that with the 2 mm-thick GFRP specimen. Since the ultrasonic transducer induced strain levels of under 2% in the GFRP specimen-support system, the effect of specimen thickness on the stiffness of this system was considerable and resulted in significant differences in the development of erosion damage, which can be observed in Figs. 12 and 13.

3.3.4. Effect of acoustic impedance

This section investigates the relationship between the acoustic impedance and the response of GFRP, glass and epoxy to cavitation erosion. For meaningful comparison between different materials, clause 11.3 in ASTM G32-16 standard [2] recommends using cumulative exposure times required to reach cumulative MDEs of 50, 100 and 200 μm . This method was not suitable as Epoxy reached only a cumulative MDE of 112 μm (see Fig. 8). Another method suggested in clause 11.4.1 in ASTM G32-16 [2] is based on the use of the maximum rate of erosion. This method was not suitable either because both epoxy and glass were still in the maximum erosion rate stage at the end of the tests (see Fig. 8). As a result, the maximum erosion rates of these materials could not be evaluated accurately. As a possible alternative, clause 11.5 in ASTM G32-16 [2] recommends using the instantaneous erosion rate. Fig. 15 presents the development of the instantaneous erosion rate with cumulative exposure time for four GFRP sheets, pure glass and pure epoxy. The values of the instantaneous erosion rates were calculated based on the data in Figs. 6 and 8. As can be seen, each curve in Fig. 15 has a clear maximum, the values of which can be used in the comparison of different materials.

Experimental data describing the specific acoustic impedance and the response to ultrasonic cavitation erosion (in terms of the maximum instantaneous erosion rate) are shown Fig. 16, where the average values are given with 95% confidence intervals derived using Student's t distribution for each GFRP sheet and for the pure epoxy. The specific acoustic impedance of glass was assumed equal $13 \times 10^6 \text{ Pa}\cdot\text{s}/\text{m}$ [28]. As can be seen, higher acoustic impedance corresponds to higher erosion damage in the materials considered. This conclusion is supported by Hattori and Itoh [7] and Chi et al. [29] findings, where composites with lower acoustic impedance demonstrated higher resistance to cavitation erosion due to lower impact energy absorption. Regression analysis of the data in Fig. 16 allowed for formulation of a linear relationship between the acoustic impedance (z) and the maximum instantaneous erosion rate ($MIER$):

$$z = 0.0158 MIER + 1.4492 \tag{3}$$

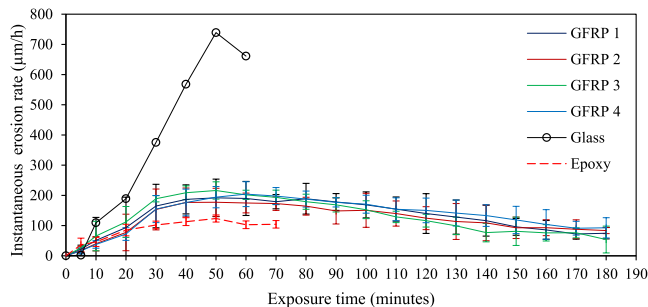


Fig. 15. Instantaneous erosion rate versus cumulative exposure time for GFRP, pure glass and pure epoxy specimens subjected to ultrasonic cavitation erosion on an aluminium block in reasonably degassed water. Edges of GFRP specimens were covered with copper tape. Average results are shown with a 95% confidence interval derived using Student's t distribution.

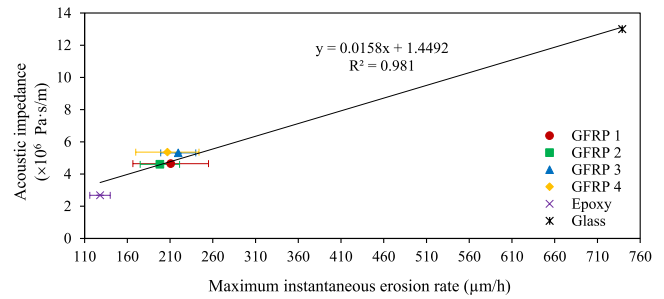


Fig. 16. Acoustic impedance versus maximum instantaneous erosion rate in GFRP composite, pure epoxy and pure glass. Average results are shown with a 95% confidence interval derived using Student's t distribution.

where z is in ($\times 10^6$) Pa·s/m and $MIER$ is in $\mu\text{m}/\text{h}$. It is necessary to note that further experimental investigation is required to fill the data gap between $MIER$ values of 260 μm and 720 μm for the relationship in Eq. (3) to become more reliable.

3.3.5. Effect of tensile strength

Fig. 17 illustrates the effect of specimen tensile strength on the ultrasonic cavitation erosion damage (in terms of the maximum instantaneous erosion rate). The average tensile strength of GFRP sheets (in 0° fibre orientation) was taken from Table 3. The tensile strength of epoxy was taken equal to 72.8 MPa (see discussion in Section 2.2). The average values of the maximum instantaneous erosion rate are shown together with 95% confidence intervals derived using Student's t distribution for each GFRP sheet and pure epoxy. It is important to note that a possible effect of specimen preparation technique on the results of different tests (i.e., ultrasonic cavitation erosion and tensile tests) was eliminated by cutting the specimens from the same GFRP or pure epoxy sheets using the same equipment and method. For the measured density of $1158 \text{ kg}/\text{m}^3$ (see Section 2.2), the tensile strength the pure epoxy specimens was evaluated at about 73 MPa using interpolation of the ranges of tensile strength and density provided by the manufacturer (see Table 4). It should be noted that such inaccurate estimation of tensile strength was considered suitable for the purposes of current discussion. The tensile strength of glass varies widely depending on the manufacturing process. Therefore, a value of 41 MPa was assumed in this discussion, which is typical of the tensile strength of annealed soda-lime-silica float glass. The data in Fig. 17 does not show any clear relationship between the two parameters considered. However, the tensile strength of float glass is not representative of the tensile strength of E-glass fibres, which varies between 3100 and 3800 MPa [30]. If the middle value of 3400 MPa is adopted, a linear relationship between the tensile strength (f_u) and the maximum instantaneous erosion rate ($MIER$) could be established using regression analysis, i.e.,

$$f_u = 5.2315 MIER - 447.49 \tag{4}$$

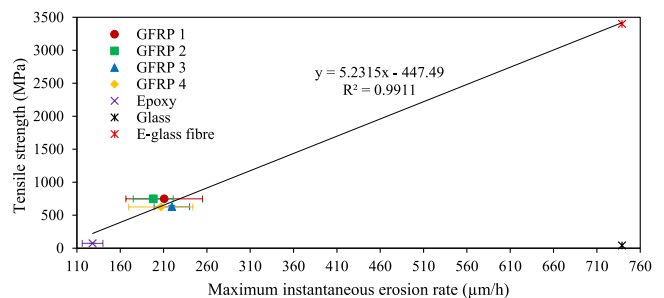


Fig. 17. Tensile strength versus maximum instantaneous erosion rate in GFRP composite, pure epoxy and pure glass. Average results are shown with a 95% confidence interval derived using Student's t distribution.

where f_{ti} is in MPa and $MIER$ is in $\mu\text{m}/\text{h}$. It is important to stress that Eq. (4) is speculative as it was derived based on an assumed tensile strength and by ignoring the differences in the cavitation erosion process in float glass sheet and E-glass fibres. Further experimental investigation is required for formulating an accurate expression. It should be noted that a non-linear relationship can also be established between Young's modulus and $MIER$.

3.4. Development of erosion damage

The images of seven erosion stages in GFRP, pure epoxy and pure glass specimens tested using setup 2 are presented in Table 5. Additional images of erosion imprints can be found in the supporting materials on the paper webpage. Note that in the supporting materials, the erosion imprints of a 2 mm-thick GFRP specimen are shown for 20 stages of 180 min of testing, while the erosion imprints of a pure epoxy specimen are shown for 9 stages of 70 min of testing.

It can be observed from the images that cavitation erosion damage developed differently in the three specimens considered. The development of erosion imprints in the GFRP specimens was affected by mechanical properties of constituent materials, bonding properties of the matrix and internal structure of the composite (i.e., layout of bundles). By 5 min of testing, erosion damage in the GFRP specimen was mostly concentrated in a few regions above fibre bundles (distinguished by darker vertical strips in the images, see Table 5 and the supporting materials) and between bundles above binding synthetic threads, where the epoxy covering fibres and threads was removed. Both the glass fibres and synthetic threads had shallow placements within the matrix, leading to a localised increase in surface stiffness and thus its brittleness. At this testing stage, the erosion imprints could be distinguished on the pure epoxy and glass specimens and were relatively uniform. The pure epoxy specimen developed small shallow pits thinly distributed over the erosion imprint, while the pits were much deeper and denser in the pure glass specimen. By 10 min, erosion damage spread over most binding threads and fibre bundles. Some binding threads and shallow fibres were removed. The pits in the erosion imprint of the pure epoxy specimen became denser and deeper (indicated by the darker colour of the imprint), while the pure glass specimen was already heavily damaged by large, very dense pits signifying the removal of surface material. By 20 min, the erosion imprint could be distinguished on the GFRP specimen. Large areas of fibre bundles were uncovered, and a fibre removal process was established, which accelerated the erosion process (see Figs. 7 and 15). The pure epoxy specimen developed large deep pits and a network of surface cracks. It should be noted that the development of the surface crack network could have also been driven by high-temperature gradients and high local temperatures created at the specimen surface during the operation of the ultrasonic transducer. Note that pits and cracks in the surface epoxy of a GFRP specimen can be observed in Fig. 18. The entire surface of the erosion imprint of the pure glass specimen was heavily damaged and developed a complex rough structure. Over the next 40 min, the fibre bundles in the erosion imprint of the GFRP specimens were uncovered and large amounts of fibres were removed, creating deep trenches while leaving the epoxy between fibres initially relatively intact and chipping it off in places at a later stage. The effect of trenching can be seen in Fig. 18 (especially in Fig. 18b). In the pure epoxy specimen, small parts of surface epoxy between cracks were gradually removed and the pits became denser and deeper. The erosion imprint of the pure glass specimen became gradually rougher and deeper as more damage developed. Eventually, a very complex structure developed at the erosion imprint of the pure glass specimen due to significant material removal. Both the pure epoxy and glass erosion imprints became 'flaky', where the glass flakes were much larger and less dense. The flakes were created by the removal of adjacent surface material and undermining by cavitation. A similar phenomenon was observed by Guobys et al. [6]. The erosion processes in the pure epoxy

and pure glass specimens were analogous to the ones in the GFRP composite, in which fibres were removed in large bunches, while the epoxy was initially less damaged. The undermining capability of cavitation was also observed in the GFRP composite. Cavitation undermined the epoxy between fibre bundles after the bundles were sufficiently eroded. The undermining process resulted in creating overhangs and chipping off large pieces of the epoxy. Furthermore, undermining occurred in eroded trenches in fibre bundles and created long bridges of glass fibres in the direction of bundles. These bridges were removed at a later erosion stage. This process has been discussed in Ref. [6] and supported by X-ray microtomography images.

The glass specimen was damaged the most, while the pure epoxy specimen was damaged the least (see the erosion imprints at 60 min of exposure in Table 5. This conclusion is supported by the MDE data in Fig. 8. As a result, the pure epoxy and glass specimens represent limits for the internal material composition of the GFRP composite. The GFRP composite responded to cavitation erosion similarly to the pure epoxy until the epoxy cover was removed. It should be noted that the sheet of float glass responded to cavitation erosion differently than individual E-glass fibres. As a result, the comparison of the cavitation erosion processes in GFRP composite and float glass can only be indicative. A more detailed description of the process of ultrasonic cavitation erosion of GFRP specimens (including microscope and X-ray computed microtomography observations) can be found in Guobys et al. [6].

Surface hardness of polymers can be correlated with the cumulative erosion rate [31]. Table 3 shows the Shore D hardness of above (S_B) and between (S_E) fibre bundles in the dry GFRP sheets. As can be seen, S_B is larger than S_E in all cases. The average S_B is 92.4 HD, while the average S_E is 87.6 HD. The difference in hardness ranges between 2.2% and 7.5%, giving about 5.5% average. It should be noted that Shore D Durometer measurements above 90 HD are not reliable [16]. However, they can be used as an indication of higher hardness of GFRP surface above fibre bundles. The comparison of the S_B and S_E values and the process of cavitation erosion of GFRP composite suggests that harder (and therefore more brittle) parts of the GFRP surface (i.e., above fibre bundles) suffered higher erosion damage. The surface hardness of the pure epoxy specimens was 84.5 HD, which is lower than that of the GFRP composite. The pure glass specimen had the highest hardness amongst the three materials considered. More brittle and thus stiffer surfaces develop higher cavitation erosion damage because more energy produced by collapsing bubbles is spent on cracking and crashing of surface material rather than on its deformation. This explains the lowest cumulative MDE and erosion rate in the pure epoxy specimens and the highest ones in the pure glass specimen reported in Figs. 8, Figs. 9 and 15.


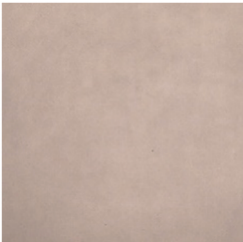

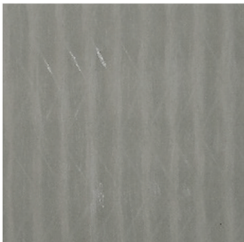
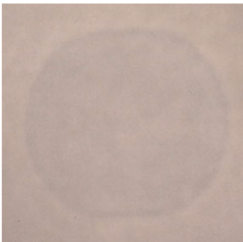
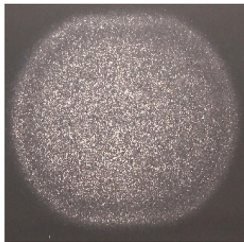
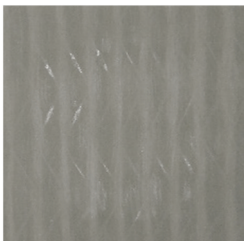
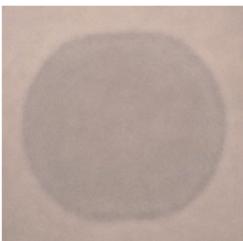
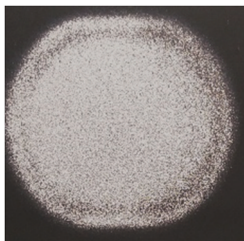

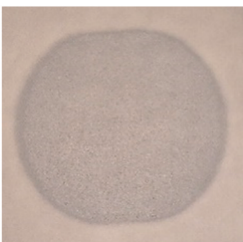
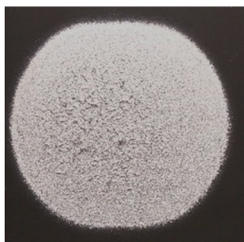

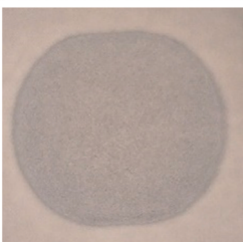
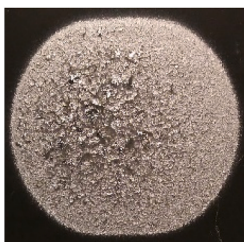

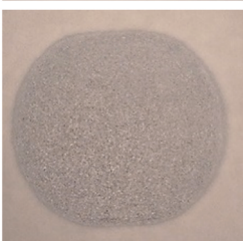

Fig. 18 shows regions of erosion imprints of GFRP surfaces after 60 and 180 min of testing. As can be seen, erosion borrowed into fibre bundles leaving parts of the epoxy cover relatively undamaged. Fig. 18a depicts an exposed fibre bundle with large number of fibres already removed. At 60-min exposure, the fibre removal process was accompanied by high erosion rate (see Figs. 7 and 15). Fig. 18b shows a multi-layered structure of a highly eroded fibre bundle. The photoelasticity phenomenon is clearly visible on many ends of broken fibres in Fig. 18. This phenomenon is indicated by rainbow colours and signifies the presence of residual strain in the fibres. It should be noted that photoelasticity was visible because of the polarised light used by the microscope for specimen illumination.

4. Conclusions

This paper investigated the response of glass fibre reinforced polymer (GFRP) composites to ultrasonic cavitation erosion and the influence of several parameters associated with the experimental setup, testing procedure and specimen material properties on the erosion process. The experimental results can be summarised as following.


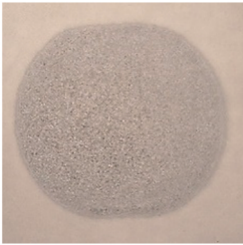
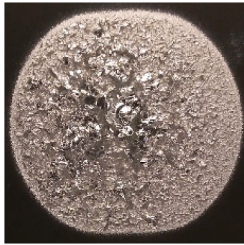

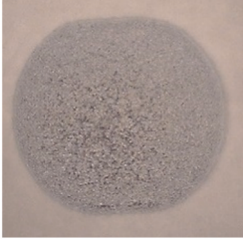
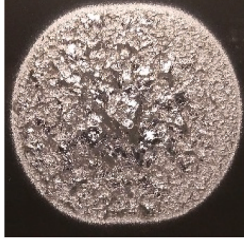
- Water purity influenced water absorption of GFRP composites but had an insignificant effect on their ultrasonic cavitation erosion.
- The highest water absorption rate occurred during the initial 24 h of saturation regardless specimens testing conditions. Covering specimen edges with epoxy should be avoided during cavitation erosion testing because it increases water absorption.
- Micro-deformations in GFRP composites induced by the ultrasonic field accelerated water intake in unconditioned (dry) specimens during the initial testing stage, resulting in an initial specimen mass gain. Therefore, preconditioning GFRP composite before ultrasonic cavitation erosion testing is essential for the accurate recording of erosion damage.

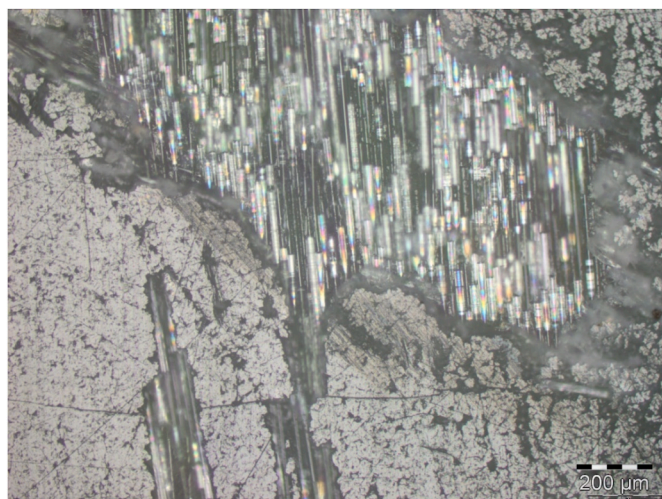
Table 5
Erosion imprints on specimen surfaces at different testing stages.

Minutes	GFRP	Epoxy	Glass
0			
5			
10			
20			
30			
40			

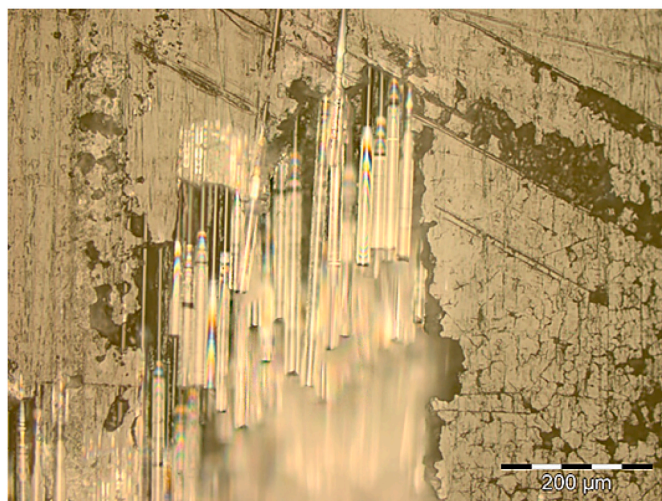
(continued on next page)

Table 5 (continued)

Minutes	GFRP	Epoxy	Glass
50			
60			



(a)



(b)

Fig. 18. (a) GFRP specimen surface after 60 min exposure to an ultrasonic cavitation field, showing cavitation erosion localisation at a binding synthetic thread in a fibre bundle region. (b) GFRP specimen surface after 180 min exposure to an ultrasonic cavitation field, showing uncovered and eroded glass fibres boundary under a fine epoxy covering layer.

- GFRP composite erosion was mostly insensitive to the content of dissolved gas in the testing liquid, while Stainless Steel 316 (SS316) was highly sensitive to it. This was attributed to different rates and uniformity of the erosion process. The GFRP composites eroded non-uniformly at a relatively high rate, while the SS316 erosion was reasonably slow and uniform.
- The stiffness of the specimen-support system influenced the process of ultrasonic cavitation erosion through its effect on the vibration introduced by the pressure fluctuations in the ultrasonic field. A larger amplitude of vibration reduced the number of bubbles that collapsed close enough to the specimen surface to cause damage. GFRP specimens tested on more flexible supports developed significantly less erosion damage than specimens tested on stiff support. Thicker GFRP specimens were more damaged by cavitation than thinner GFRP specimens. Furthermore, specimen stiffness was especially important for testing on flexible supports. Gluing GFRP specimens to stiff support (e.g., metal plate or block) can be recommended as means of eliminating the effect of the specimen-support system stiffness on the ultrasonic cavitation erosion process. However, this method cannot be used when scanning GFRP specimens with X-ray computed microtomography is planned as part of the testing procedure.
- Materials with higher specific acoustic impedance, higher tensile strength and higher surfaces hardness developed higher erosion damage.
- Pure glass eroded the fastest due to high surface brittleness and hardness. Pure epoxy was the most resistant to cavitation. The GFRP composite resisted cavitation erosion mainly by the epoxy matrix.
- Erosion damaged developed slowly in GFRP composite while removing the epoxy layer covering fibre bundles. Fast removal of fibres by cavitation accelerated the erosion. At later testing stages, the erosion rate slowed down because the distance between the transducer tip and the specimen surface increased and the erosion imprint developed a complex multilevel structure.
- The erosion imprints of both pure epoxy and glass were ‘flaky’ by the end of the tests. The epoxy developed deep pits and small flakes, while the glass developed a complex imprint structure with large flakes. The erosion imprint of the GFRP composite showed the features observed during the testing of both the epoxy and glass. The epoxy-filled gaps eroded slowly and were relatively smooth, while the fibre bundles eroded relatively quickly and had a complex structure dominated by trenches in the direction of fibre bundles. Localisation of the erosion process led to deep borrowing of cavitation into the surface followed by undermining surface material.

Author agreement statement

We the undersigned declare that this manuscript is original, has not been published before and is not currently being considered for publication elsewhere. We confirm that the manuscript has been read and approved by all named authors and that there are no other persons who satisfied the criteria for authorship but are not listed. We further confirm that the order of authors listed in the manuscript has been approved by all of us. We understand that the Corresponding Author is the sole contact for the Editorial process. He/she is responsible for communicating with the other authors about progress, submissions of revisions and final approval of proofs.

Declaration of competing interest

All authors of a manuscript titled "Factors affecting the procedure for testing cavitation erosion of GFRP composites using an ultrasonic transducer" declare that they have no known competing financial interests or personal relationships that could have appeared to influence the work reported in this paper. Also, the authors declare that there are no financial interests/personal relationships which may be considered as potential competing interests.

Data availability

Data will be made available on request.

Appendix A. Supplementary data

Supplementary data to this article can be found online at <https://doi.org/10.1016/j.wear.2023.205059>.

References

- [1] L. Chernin, D. Val, Probabilistic prediction of cavitation on rotor blades of tidal stream turbines, *Renew. Energy* 113 (2017) 688–696.
- [2] ASTM G32-16, Standard Test Method for Cavitation Erosion Using Vibratory Apparatus, ASTM International., West Conshohocken, PA, 2016.
- [3] D. Hammond, M. Amateau, R. Queeney, Cavitation erosion performance of fiber reinforced composites, *J. Compos. Mater.* 27 (16) (1993) 1522–1544.
- [4] V. Caccese, K. Light, K. Berube, Cavitation erosion resistance of various material systems, *Ships Offshore Struct.* 1 (4) (2006) 309–322.
- [5] T. Yamatogi, H. Murayama, K. Uzawa, K. Kageyama, N. Watanabe, Study on cavitation erosion of composite materials for marine propeller, in: ICCM-1, 2009.
- [6] R. Guobys, A. Rodríguez, L. Chernin, Cavitation erosion performance of unidirectional glass fibre reinforced composites, *Compos. B Eng.* 177 (15 November) (2019), 107374, <https://doi.org/10.1016/j.compositesb.2019.107374>, 12pp.
- [7] S. Hattori, T. Itoh, Cavitation erosion resistance of plastics, *Wear* 271 (7–8) (2011) 1103–1108.
- [8] N. Rahman, A. Hassan, R. Yahya, R. Lafia-Araga, Impact properties of glass-fiber/polypropylene composites: the influence of fiber loading, specimen geometry and test temperature, *Fibers Polym.* 14 (11) (2013) 1877–1885.
- [9] M. Minnaert, XVI. On musical air-bubbles and the sounds of running water, *London, Edinburgh Dublin Phil. Mag. J. Sci.* 16 (104) (1933) 235–248.
- [10] H. Feng, G. Barbosa-Cánovas, J. Weiss, *Ultrasound Technologies for Food and Bioprocessing*, Springer, New York, 2011.
- [11] L. Bai, W. Xu, F. Zhang, N. Li, Y. Zhang, D. Huang, Cavitation characteristics of pit structure in ultrasonic field, *Sci. China E* 52 (7) (2009) 1974–1980.
- [12] National Institutes of Health (USA), Image processing software ImageJ [online] Available at: <https://imagej.nih.gov/ij/>. (Accessed 11 February 2023).
- [13] Graphics Volume, VGSTUDIO MAX: high-end software for CT data [online] Available at: <https://www.volumegraphics.com/en/products/vgstudio-max.html>. (Accessed 11 February 2023).
- [14] S. Hattori, R. Ishikura, Q. Zhang, Construction of database on cavitation erosion and analyses of carbon steel data, *Wear* 257 (2004) 1022–1029.
- [15] ASTM D3039/D3039M-17, Standard Test Method for Tensile Properties of Polymer Matrix Composite Materials, ASTM International, West Conshohocken, PA, 2017.
- [16] ASTM D2240-15e1, Standard Test Method for Rubber Property - Durometer Hardness, ASTM International., West Conshohocken, PA, 2015.
- [17] K. Liao, C. Schultheisz, D. Hunston, Long-term environmental fatigue of pultruded glass-fiber-reinforced composites under flexural loading, *Int. J. Fatig.* 21 (5) (1999) 485–495.
- [18] F. Buehler, J. Seferis, Effect of reinforcement and solvent content on moisture absorption in epoxy composite materials, *Compos. Appl. Sci. Manuf.* 31 (7) (2000) 741–748.
- [19] F. Ellyin, C. Rohrbacher, The influence of aqueous environment, temperature and cyclic loading on glass-fibre/epoxy composite laminates, *J. Reinforc. Plast. Compos.* 22 (7) (2003) 615–636.
- [20] B. Abdel-Magid, S. Ziaee, K. Gass, M. Schneider, The combined effects of load, moisture and temperature on the properties of E-glass/epoxy composites, *Compos. Struct.* 71 (3–4) (2005) 320–326.
- [21] W. Chow, Water absorption of epoxy/glass fiber/organo-montmorillonite nanocomposites, *Express Polym. Lett.* 1 (2) (2007) 104–108.
- [22] A. Chatterjee, J. Gillespie, Moisture absorption behaviour of epoxies and their S2 glass composites, *J. Appl. Polym. Sci.* 108 (6) (2008) 3942–3951.
- [23] A. Mourad, B. Abdel-Magid, T. El-Maaddawy, M. Grami, Effect of seawater and warm environment on glass/epoxy and glass/polyurethane composites, *Appl. Compos. Mater.* 17 (5) (2010) 557–573.
- [24] L. Bian, J. Xiao, J. Zeng, S. Xing, Effects of seawater immersion on water absorption and mechanical properties of GFRP composites, *J. Compos. Mater.* 46 (25) (2012) 3151–3162.
- [25] T. Sathishkumar, S. Satheshkumar, J. Naveen, Glass fiber-reinforced polymer composites - a review, *J. Reinforc. Plast. Compos.* 33 (13) (2014) 1258–1275.
- [26] ASTM D5229/D5229M - 14, Standard Test Method for Moisture Absorption Properties and Equilibrium Conditioning of Polymer Matrix Composite Materials, ASTM International., West Conshohocken, PA, 2014.
- [27] ASTM D570 - 98(2010)e1, Standard Test Method for Water Absorption of Plastics, ASTM International, West Conshohocken, PA, 2015.
- [28] F.J. Álvarez Franco, Fundamentals of airborne acoustic positioning systems, in: Jordi Conesa, Antoni Pérez-Navarro, Joaquín Torres-Sospedra, Raul Montoliu (Eds.), *Intelligent Data-Centric Systems, Geographical and Fingerprinting Data to Create Systems for Indoor Positioning and Indoor/Outdoor Navigation*, vol. 2019, Academic Press, 2019, pp. 335–351, <https://doi.org/10.1016/B978-0-12-813189-3.00017-4>.
- [29] S. Chi, J. Park, M. Shon, Study on cavitation erosion resistance and surface topologies of various coating materials used in shipbuilding industry, *J. Ind. Eng. Chem.* 26 (2015) 384–389.
- [30] F. Wallenberger, P. Bingham, *Fiberglass and Glass Technology*, Springer, New York, 2010.
- [31] H. Böhm, S. Betz, A. Ball, The wear resistance of polymers, *Tribol. Int.* 23 (6) (1990) 399–406.